# ANALYSIS ON FLOW AROUND A SPHERE AT HIGH MACH NUMBER, LOW REYNOLDS NUMBER AND ADIABATIC CONDITION FOR HIGH ACCURACY ANALYSIS OF GAS PARTICLE FLOWS

## T. NAGATA[*], T. NONOMURA[†], S.TAKAHASHI[†], Y.MIZUNO[†] AND K.FUKUDA[†]

[*] Tokai University, 4-1-1, Kitakaname, Hiratsuka, Japan, e-mail: 1beu2216@mail.tokai-u.jp

[†]Japan Aerospace Exploration Agency, Institute of Space and Astronautical Science (JAXA/ISAS), 3-1-1, Yoshinodai, Sagamihara, Japan, e-mail: nonomura@flab.isas.jaxa.jp

[†]Tokai University, 4-1-1, Kitakaname, Hiratsuka, Japan, e-mail: takahasi@mail.tokai-u.jp

[†]Tokai University, 4-1-1, Kitakaname, Hiratsuka, Japan, e-mail: 1beu2104@mail.tokai-u.jp

[†]Tokai University, 4-1-1, Kitakaname, Hiratsuka, Japan, e-mail: fukuda@mail.tokai-u.jp

**Key words:** High Mach number and Low Reynolds number flow, Drag model

**Abstract.** This study analyses gas particle flow around a sphere under an adiabatic condition at high Mach number and low Reynolds number by direct numerical simulation of the three–dimensional compressible Navier–Stokes equation to investigate flow properties. The calculation was performed on a boundary-fitted coordinate system with a high-order scheme of sufficient accuracy. Analysis is conducted by assuming a rigid sphere with a Reynolds number based on the diameter of the sphere, and the free-stream velocity set between 50 and 300 and a free-stream Mach number set between 0.3 and 2.0. The effect of the Mach number on the flow properties and drag coefficient are discussed. The calculation shows the following results: 1) unsteady fluctuation of the hydrodynamic force becomes smaller as the Mach number increases, 2) the drag coefficient increases along with the Mach number due to an increase in the pressure drag by the shock-wave, and 3) an accurate prediction of the drag coefficient in the supersonic regime using traditional models might be difficult.

## 1 INTRODUCTION

Certain acoustic phenomena are caused by fluid behavior. In particular, the exhaust gas from a rocket engine generates a strong acoustic wave. The acoustic waves reflected from the ground surface and launch facility, causes vibration of the payload in the fairing. Therefore, prediction and reduction of the acoustic level at lift-off are necessary. Traditionally, the acoustic level has been predicted by a semi-empirical method such as NASA SP-8072 [1] and subscale tests [2]. NASA SP-8072 is based on a large amount of flight data and results of static firing tests that were conducted by the organization in the United States; it does not

consider the effects of the launch pad and facility because NASA SP-8072 assumes that sound sources are distributed along a free jet. Therefore, it is necessary to create a model to modify the prediction results for each launch pad. Hence, NASA SP-8072 is not suitable as a design tool for new launch pads. Moreover, static firing tests are costly. Recent, predictions of the acoustic level using computational fluid dynamics (CFD) are required for these reasons.

The alumina particles released from solid rocket motors and water droplets introduced by water injection to the exhaust gas might attenuate the acoustic wave. However, the attenuation mechanism is not well known. Recently, the effects of water droplets have been verified [3,4]. In previous studies, Tsutsumi et al. [5,6] performed analyses in consideration of the effects of the launch facility and the flame deflector plate. In addition, an analysis considering the difference of the components of the exhaust and the atmosphere was performed by Nonomura et al. [7]. Consequently, the acoustic phenomena have been clarified. If it becomes possible to consider the effect of the particles on the analysis, it is expected that acoustic wave level prediction using CFD will become more accurate than predictions under the present method. The diameters of the alumina particles released from solid rocket motors are 30-200 μm [8], and the exhaust gas is a supersonic flow. Therefore, flow around each particle has a high Mach number and a low Reynolds number. Accordingly, a drag model under a high Mach number and a low Reynolds number condition is necessary to perform analysis that considers the influence of the particle on the jet flow. In this study, direct numerical simulation (DNS) of the flow around a sphere at high Mach number and low Reynolds number is conducted to construct a subgrid scale and body-force models that consider the influence of particles. Analyses are performed by assuming that the alumina particle is a rigid sphere; the Reynolds number based on the diameter of the sphere and the free-stream velocity is set between 50 and 300, the free-stream Mach number is set between 0.3 and 2.0 (Table 1).

## 2  ANALYTICAL METHOD

### 2.1  Computational grid

A boundary-fitted grid is adopted for this computation. The dimensions of the grid are $\xi \times \eta \times \zeta = 107 \times 48 \times 177$ points, with 909,072 grid points. The boundary condition at the sphere's surface is nonslip and adiabatic. At the boundaries of the $\xi$ and $\eta$ directions, periodic boundary conditions with three overlapped grid points are imposed (Figure 1). The diameter of the analysis region is 100 times that of the sphere. Figure 1 shows a computational grid. The sphere's diameter is 1D. The grid size of the $\zeta$ direction is stretched by 1.03 times from the minimum grid width within 15D of the origin, and the grid size is constant after it reaches 0.2D. In regions 15D or more away from the origin point, the grid size is stretched by 1.2 times toward the outer boundary. The minimum grid size is calculated by the following formula [9.]:

$$dr_{\min} = \frac{1.13}{\sqrt{\mathrm{Re} \times 10.0}} . \tag{1}$$

In this study, the minimum grid for all calculations is fixed with the size determined by assuming that the Reynolds number is 300.

**Table 1**: Analysis case

| Reynolds number | Mach number | Cace. |
|---|---|---|
| 50 | 0.30 | Re050M030 |
| | 0.80 | Re050M080 |
| | 1.20 | Re050M120 |
| | 2.00 | Re050M200 |
| 100 | 0.30 | Re100M030 |
| | 0.80 | Re100M080 |
| | 1.20 | Re100M120 |
| | 2.00 | Re100M200 |
| 150 | 0.30 | Re150M030 |
| | 0.80 | Re150M080 |
| | 1.20 | Re150M120 |
| | 2.00 | Re150M200 |
| 200 | 0.30 | Re200M030 |
| | 0.80 | Re200M080 |
| | 1.20 | Re200M120 |
| | 2.00 | Re200M200 |
| 250 | 0.30 | Re200M030 |
| | 0.80 | Re250M080 |
| | 1.20 | Re250M120 |
| | 2.00 | Re250M200 |
| 300 | 0.30 | Re300M030 |
| | 0.70 | Re300M080 |
| | 0.80 | Re300M120 |
| | 0.95 | Re300M200 |
| | 1.05 | Re300M030 |
| | 1.20 | Re300M080 |
| | 1.50 | Re300M120 |
| | 2.00 | Re300M200 |
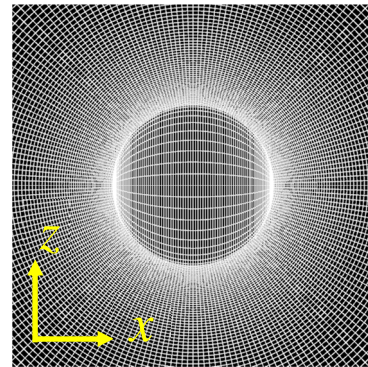


a. Close view
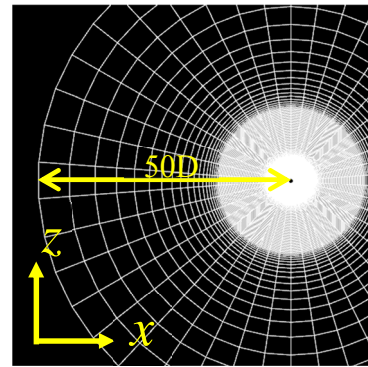


b. Far view

**Figure 1**: Computational grid

## 2.2 Computational method

In this calculation, the Navier–Stokes equation is employed as the governing equation. The equation is non-dimensionalized by the free-stream speed of sound, the density, and the diameter of the sphere. The convection term is evaluated by the WENO-CU6-FP [10] method, the viscous term by the sixth-order central difference method, and time integration is performed by the third-order TVD Runge–Kutta method. WENO-CU6-FP is the WENO method satisfying the geometric conservation laws in the curvilinear coordinate system, which was proposed by Nonomura et al. [10]. This scheme can preserve the free-stream. In this study, the central difference component of the WENO-CU6-FP scheme is replaced by one of the splitting type [11] in order to better stabilize the calculation.

## 3 COMPUTATIONAL RESULT OF FLOW AROUND A SPHERE

### 3.1 Flow regime

### 3.1.1 Pressure coefficient distribution and vortex structure

Figures 2 and 3 are the snapshots of the moment field. Figure 2 shows the pressure

coefficient distribution and the stream lines. Figure 3 shows the entire view of the vortex structure visualized by the isosurface of the second invariant of a velocity gradient tensor. The threshold is set to the appropriate value for each case. From the visualization, the pressure coefficient distribution is axisymmetric and a hairpin vortex is observed in the subsonic flow. Conversely, the pressure coefficient distribution becomes almost symmetric under transonic and supersonic conditions, and a clear hairpin vortex structure disappears as the Mach number increases. The hairpin vortex structure also disappears at Mach 0.95. In addition, at Mach 0.95, the shock-wave is formed at the downstream side of the sphere.

### 3.1.2 Separation point and separation length

The separation point is probed by considering the velocity gradient on the sphere surface. In this study, the separation point is expressed as the degree from the $x$ axis, as shown in Figure 4. Separation length is expressed as the distance from the sphere's surface to the separation regime termination. In this study, the separation length is probed by the $u$ direction component of the flow velocity on the $x$ axis of the downstream side. The end of the separation region is set to be the position where the sign of the $u$ component velocity switches (Figure 4). Figures 5 and 6 show the separation point and separation length of the time-averaged field, respectively. The separation point location and separation length change significantly in the transonic region. The separation point moves to the upstream side at subsonic flow and to the downstream side from transonic to supersonic flow. Conversely, the separation length increases under the subsonic and transonic flows and decreases at the supersonic flow. The separation length rapidly increases at Mach 0.95. In addition, the separation length is hardly changed; therefore, the separation point is influenced by the presence or absence of the shock-wave (i.e., $M < 1$ or $M > 1$), and the separation length is gradually influenced by the effects of compressibility. Hence, there is a need to discuss the interference of the shock-wave with the wake.
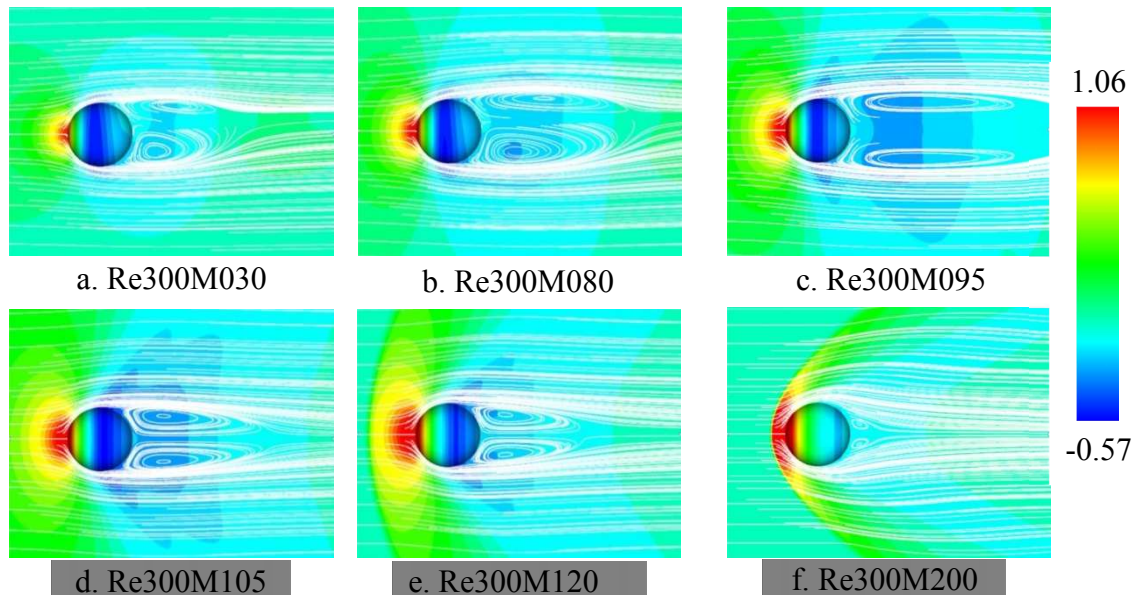


a. Re300M030     b. Re300M080     c. Re300M095

d. Re300M105     e. Re300M120     f. Re300M200

**Figure 2**: Pressure coefficient distribution and streamline

a. Re300M030

b. Re300M070

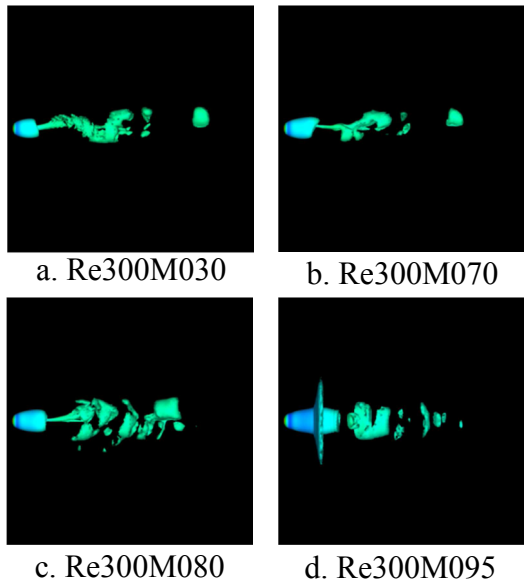c. Re300M080

d. Re300M095

**Figure 3**: Isosurfaces of the second invariant of the velocity gradient tensor
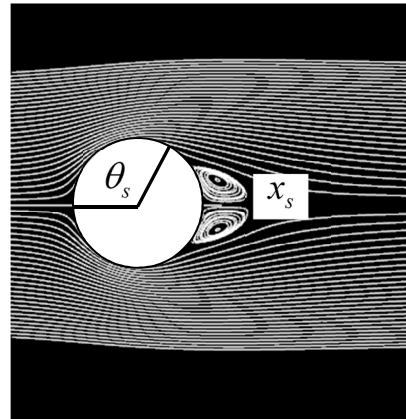


**Figure 4**: Separation point $\theta_s$ and separation length $x_s$
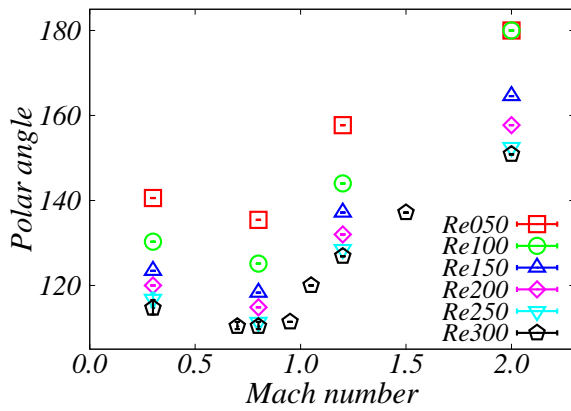


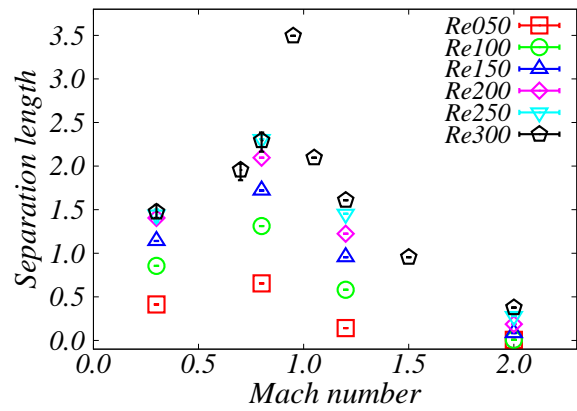**Figure 5**: Separation point
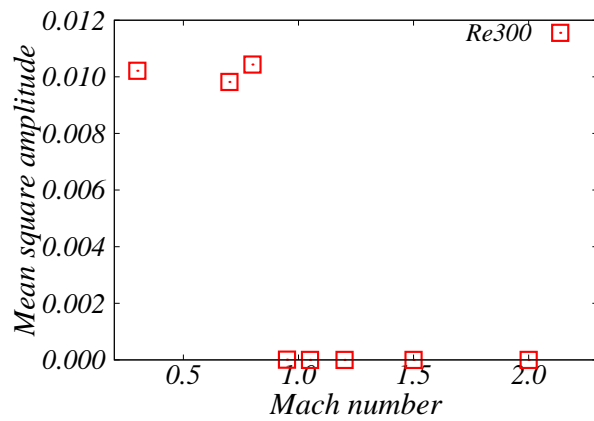


**Figure 6**: Separation length



**Figure 7**: Mean square amplitude
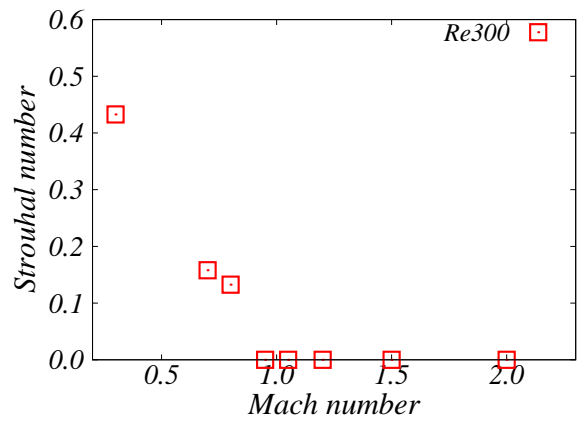

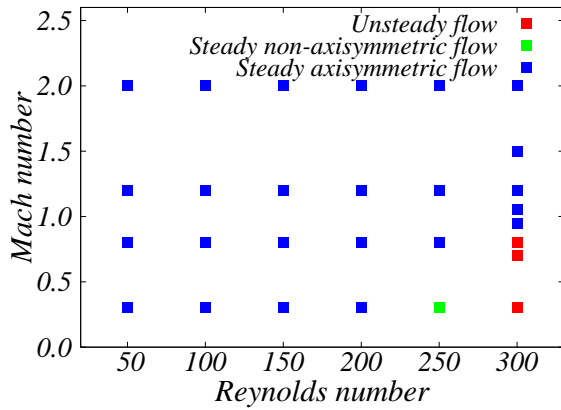
**Figure 8**: Strouhal number
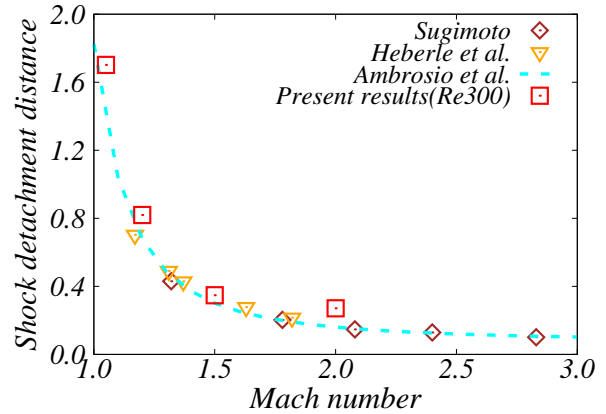
**Figure 9**: Flow regime



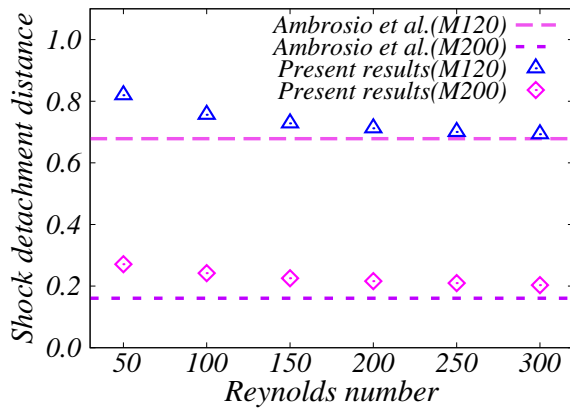**Figure 10**: Shock detachment distance at Re300



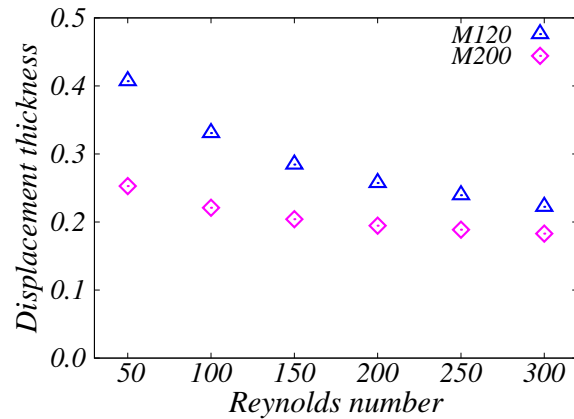**Figure 11**: Influence of the Reynolds number on the shock detachment distance



**Figure 12**: Displacement thickness

### 3.1.2 Time variation of the flow field

Figure 7 shows the root-mean-square amplitude of the lift coefficient when the Reynolds number is 300. The lift coefficient vibrates in the case of Reynolds number 300 and Mach numbers 0.3, 0.7, and 0.8. It is estimated that the phenomenon appears with the generation of the hairpin vortex. Therefore, flow fields are unsteady in these cases. Conversely, the flow fields under the transonic and supersonic conditions are steady. In addition, the root-mean-square amplitude of the lift coefficient is mostly not influenced by the Mach number at Reynolds number 300. Hence, the flow regime is influenced by the presence or absence of the shock wave. Moreover, Figure 8 shows the Strouhal number based on the lift coefficient at Reynolds number 300. The Strouhal number decreases as the Mach number increases. This shows that the fluctuation frequency of the body force is influenced by the Mach number. Figure 9 shows the flow regime of each case. The red plot shows unsteady flow, the green plot shows steady non-axisymmetric flow, and the blue plot shows the steady axisymmetric

flow. Flow becomes unsteady under the subsonic condition at Reynolds number 300. Conversely, flow becomes steady under the transonic and supersonic conditions at Reynolds number 300. In addition, when the Mach number is 0.3 and the Reynolds number is 250, there is a steady axisymmetric flow. At Mach numbers greater than 0.8, flow becomes steady and axisymmetric. Moreover, the flow regime at Mach 0.3 is the same as the results of previous studies of incompressible flow [9]. Hence, it appears that the flow field becomes steady and axisymmetric when the Mach number increases.

### 3.1.3 Shock detachment distance

Figures 10 and 11 show the comparisons of the shock detachment distance of the previous study and present results, respectively. Sugimoto et al. [12] and Haberle et al. [13] showed experimental results. Ambrosio et al. [14] showed a prediction model of the shock detachment distance that was constructed from the experimental data. From Figure 11, the present results agree well with Ambrosio et al. at Reynolds number 300. The model does not include the effects of the Reynolds number. The present results show that the shock standing distance increases as the Reynolds number decreases. Figure 12 shows the displacement thickness estimated by considering the flat plate boundary layer thickness. From Figure 12, the displacement thickness increases as the Reynolds number decreases. Hence, the shock detachment distance increases because the effective size of the object increases. Therefore, the fluctuation of the shock detachment distance is influenced by the thickness of the boundary layer. At low Reynolds numbers, the boundary layer is thicker than that at high Reynolds numbers. It is believed that the difference is caused by the boundary layer thickness.

### 3.2 Drag coefficient

In Figure 13–15, changes in the drag coefficients and their components as functions of the Mach number are shown. Figures 13, 14, and 15 show the drag coefficients, the pressure drag coefficients, and the viscous drag coefficients, respectively. Figure 12 shows that the drag coefficient increases as the Mach number increases. In particular, the drag coefficient increases rapidly in the transonic flow. Conversely, in the supersonic flow, the drag coefficient is hardly changed. In Figure 13, the pressure drag coefficient is influenced by the Mach number. In contrast, the viscous drag coefficient is hardly changed. In the below sections, the pressure and viscous drag coefficients will be discussed in detail.

### 3.2.1 Pressure drag coefficient

Figure 13 shows that the pressure drag coefficient increases along with the Mach number. Under the subsonic and transonic conditions, it rapidly increases. However, under the supersonic condition, it hardly changes. In addition, the pressure coefficient decreases in the low Reynolds number case of the supersonic flow. The pressure drag coefficient decrease under the subsonic condition occurs by the moving of the separation point to the upstream side. Under the transonic condition, the separation point moves to downstream side; however, the pressure drag coefficient increases. This appears to be because of the formation of the shock wave.

### 3.2.2 Viscous drag coefficient

Figure 14, illustrates that the viscous drag coefficient is hardly influenced by the Mach number. In an incompressible flow, the viscous drag coefficient is influenced by the behavior of the separation point. However, Figures 6 and 14 show a different trend. In addition, Figure 15 shows the trend of the increase in non-dimensional viscosity coefficients with increasing Mach number due to aerodynamic heating.

In subsonic flow, the separation point moves to the upstream side, and the viscous drag becomes smaller due to the decrease of the attached flow area. Therefore, the viscous drag coefficient does not change much because the increase in the viscosity coefficient excludes the effects of the separation point. Conversely, in supersonic flow, the separation point moves to the downstream side, and the viscosity coefficient increases, though the viscous drag coefficient hardly does so. This is because of the deceleration. Figure 16 shows the velocity gradient of the $u$ direction component at the one layer from the sphere surface normalized by the free-stream. From Figure 16, the velocity gradient decreases in the supersonic flow. This seems to be caused by the deceleration of the fluid at the detached shock waves. For these reasons, it is estimated that the viscous drag coefficient does not significantly increase under subsonic and supersonic conditions.
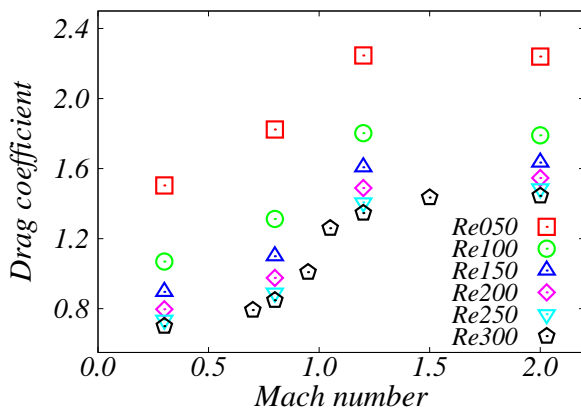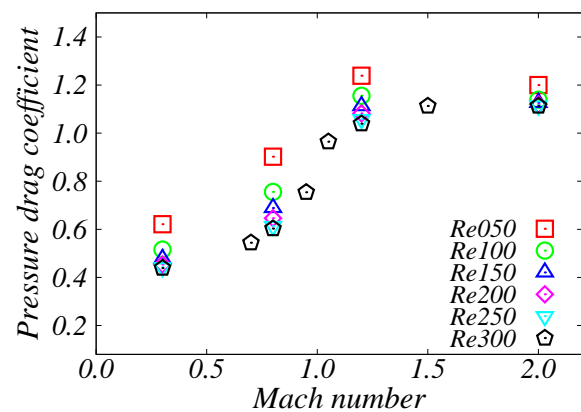


**Figure 13**: Drag coefficient
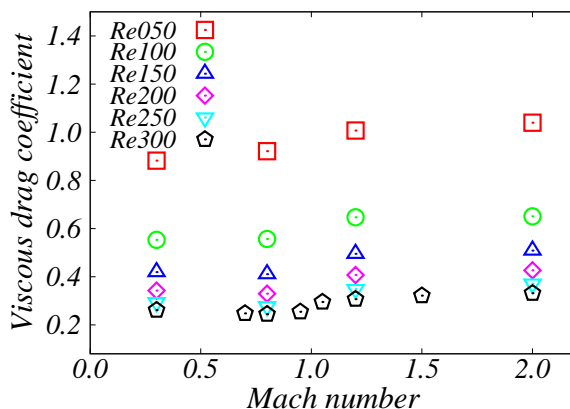


**Figure 14**: Pressure drag coefficient
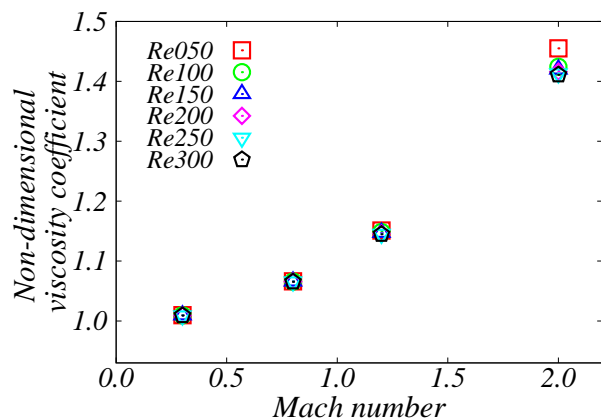


**Figure 15**: Viscous drag coefficient



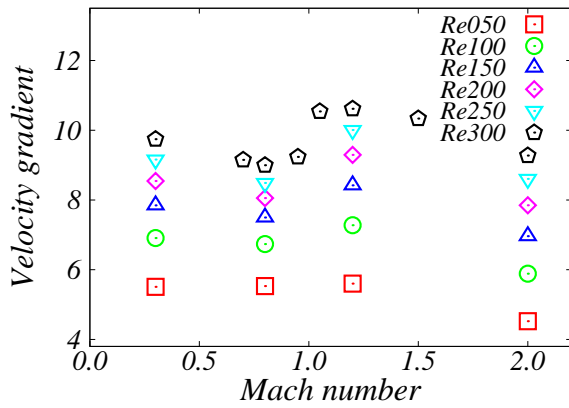**Figure 16**: Non-dimensional viscosity coefficient on the sphere surface

**Figure 17**: Mean value of the x-direction component of the velocity gradient on the sphere surface
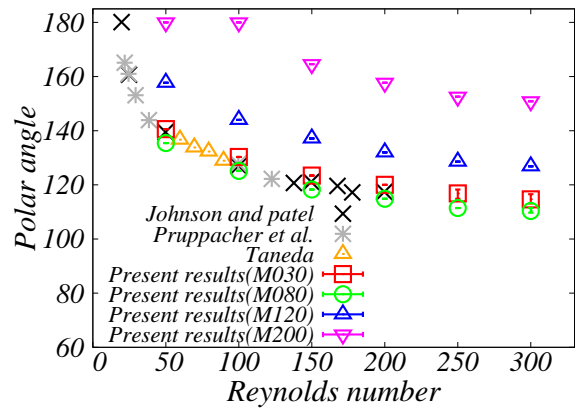


**Figure 18**: Separation points of the analysis results and the previous study results
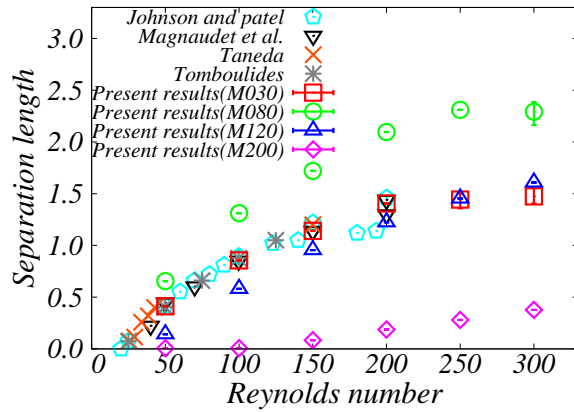


**Figure 19**: Separation lengths of the analysis results and the previous study results
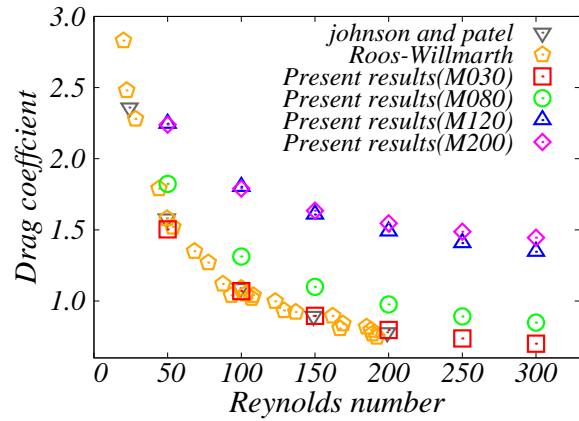


**Figure 20**: Drag coefficients of the analysis results and the previous study results
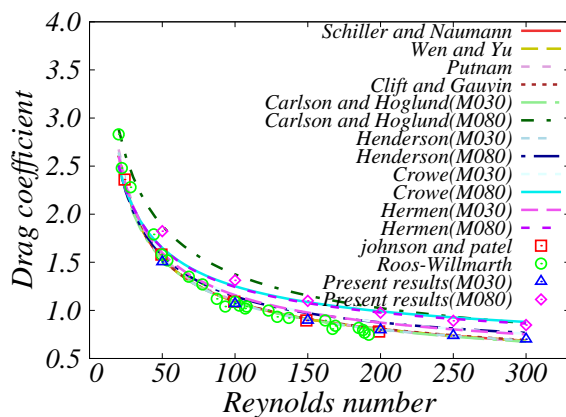


**Figure 21**: Analysis results and values predicted by drag models at the subsonic
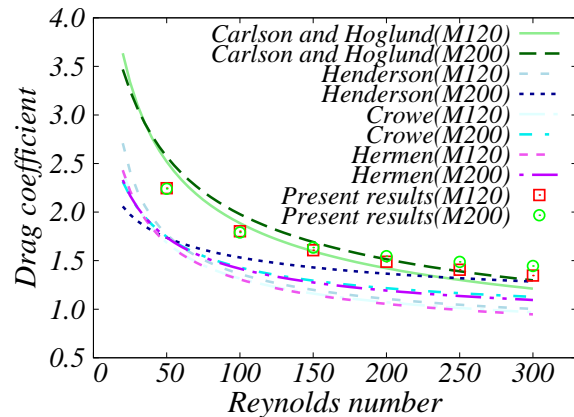


**Figure 22**: Analysis results and values predicted by drag models at the subsonic

### 3.3  Comparison with incompressible flow

#### 3.3.1  Flow regime

Under incompressible flow, the flow regime is same if the Reynolds number is matched. However, in compressible flow, both the Reynolds number and the Mach number need to be considered. Figure 17 shows a comparison of the separation point. The present results in the subsonic condition are in good agreement with incompressible results. However, the difference in the separation point becomes larger in transonic and supersonic flows. Therefore, it is estimated that the separation point is affected by the presence and intensity of the detached shock wave. Conversely, the separation length is different at Mach number 0.8 as compared with the results of the incompressible flow (Figure 18). Therefore, separation length appears to be gradually affected by the compressibility.

#### 3.3.2 Drag coefficient

Figures 19–21 show the drag coefficient. Figure 19 shows the results in the incompressible flow condition [9] along with the results of this study. At Mach 0.3, the present result is in good agreement with the results of incompressible flow studies. However, under supersonic flow, there are large differences; thus, it can be seen that there is the need to consider the Mach number when predicting the drag coefficient for high Mach number and low Reynolds number flows. Figures 20 and 21 show the comparison between the prediction values of the drag models [8, 15-18] and the present results. In Figure 20, the results of the experiment and calculation from previous studies are also shown; under subsonic flow, predicted values of drag models show good agreement with the results of this study. The model of Carlson and Hoglund [15] shows the best agreement of any model. In addition, the values predicted by the drag model that does not consider the Mach number effect also show good agreement with the results of this study. However, in the case of high Mach numbers, the difference of the drag coefficient becomes larger over the entire region. In Figure 21, under the supersonic flow condition, predicted values of the drag models do not show as good agreement as in the subsonic case. In particular, the difference between the predicted value of the drag models and present result becomes larger at low Reynolds numbers. In addition, there are differences in each drag model. Note that the Carlson and Hoglund model still shows good agreement in the supersonic case.

The model presented by Carlson and Hoglund does not consider the temperature ratio. However, it shows good agreement at all Mach numbers used in this analysis. The temperature ratio is the ratio between the temperatures of the particle and the free-stream. In this study, the calculation conditions are adiabatic at the sphere surface. Therefore, the temperature ratio is basically 1.0. However, at high Mach number flow, the sphere surface is heated by aerodynamic heating. Accordingly, in this study, particle temperature is decided by the average temperature of the sphere surface. Therefore, the cause of the large difference of the drag coefficient might be that the effects of the temperature distribution are not considered and there are problems with the calculation method. However, there is difference in the predicted value despite calculation under the same conditions. Therefore, it seems that the cause of the difference is something other than the temperature distribution. In addition, the difference becomes larger as Mach number increase. The target flow field has high Mach

number and low Reynolds number. Therefore, the measurement of the drag force is difficult. Hence, the drag model was built in a combination of the theoretical formula and indirect experimental data. Therefore, it seems that the prediction of the drag coefficient by the drag model is difficult under high Mach number and low Reynolds number conditions.

## 4   CONCLUSIONS

In this study, we performed the analyses of high Mach number and low Reynolds number flows. Consequently, we clarified the following topics: 1) As Mach number increases, unsteady fluctuation becomes weak and the separation point moves to the downstream side, 2) the drag coefficient becomes higher in the supersonic region due to the increase in the pressure drag by the detached shock-wave in the supersonic region, while the separation does not significantly affect it, and 3) the previous drag model shows good agreement with the present results in the subsonic region, while accurate prediction of the drag coefficient in the supersonic regime by traditional models might be difficult because the previous drag models are based on a model of incompressible flow and indirect experiment results.

## REFERENCES

[1] Eldred, K. M. "Acoustic Loads Generated by the Propulsion System", NASA SP-8072, (1971).

[2] Ishii, T., Tsutsumi, S., Ui, K., Tokudome, S., Ishii Y., Wada, K. and Nakamura, S., "Acoustic Measurement of 1:42 Scale Booster and Launch Pad", Proceedings of Meetings on Acoustics, Vol. 18, No. 1, pp. 040009, (2014).

[3] Fukuda, K., Tsutsumi, S., Shimizu, T., Takaki, R., and Ui, K., "Examination of Sound Suppression by Water Injection at Lift-off of Launch Vehicles", 17th AIAA/CEAS Aeroacoustics Conference, (2011).

[4] Ignatius, J. K., Sathiyavageeswaran, S., and Chakravarthy, S. R., "Hot-Flow Simulation of Aeroacoustics and Suppression by Water Injection During Rocket Liftoff", AIAA Journal, Vol. 53, No. 1, pp. 235-245, (2014), DOI: 10.2514/1.J053078.

[5] Tsutsumi, S., Shimizu, T., Takaki, R., Shima, E., Arita, M. and Fujii, K, "Numerical Study of Pressure Waves Generated by H-IIA Launch Vehicle at Lift-off", AJCPP, pp. 266-271, (2008).

[6] Tsutsumi, S., Ishii, T., Ui, K., Tokudome, S., Wada, K., "Study on Acoustic Prediction and Reduction of Epsilon Launch Vehicle at Liftoff", Journal of Spacecraft and Rockets, pp. 1-12, (2014), DOI: 10.2514/1.A33010

[7] Nonomura, T., Morizawa, S., Obayashi, S. and Fujii, K., "Computational Prediction of Acoustic Waves from a Subscale Rocket Motor", Trans. JSASS Aerospace Thec. Japan, Vol. 12, No. 29, pp. Pe_11-Pe_17, (2014).

[8] Shimada, T., Daimon, Y. and Sekino, N. "Computational Fluid Dynamics of Multiphase Flows in Solid Rocket Motors", JAXA Special Publication, JAXA-SP-05-035E, (2006).

[9] Johnson, T. A and Patel, V. C., "Flow Past a Sphere Up to a Reynolds Number of 300",

Journal of Fluid Mechanics, Vol. 378, pp. 19-70, (1999).

[10] Nonomura, T., Terakado, D., Abe, Y. and Fujii, K., "A New Technique for Freestream Preservation of Finite-Difference WENO on Curvilinear Grid", Computers & Fluids, Vol. 107, pp. 242-255, (2015).

[11] Pirozzoli, S., "Stabilized Non-dissipative Approximations of Euler Equations in Generalized Curvilinear Coordinates", Journal of Computational Physics, Vol. 230, No. 8, pp. 2997-3014, (2011).

[12] Sugimoto, M., Giken-Zappo, No. 355(1944).

[13] Heberle, W. J., Wood, P. G., and Gooderum, B. P., N.A.C.A. Tech. Note 2100 (1950).

[14] Ambrosio, A. and Wortman, A., "Stagnation Point Shock Detachment Distance for Flow Around Spheres and Cylinders", ARSJ, Vol. 32, No. 281, pp. 875-875, (1962).

[15] Carlson, J. D. and Hoglung, F. R., "Particle drag and heat transfer in rocket nozzles", AIAA Journal, Vol. 2, No. 11, pp. 1980-1984, (1964).

[16] Henderson, C. B., "Drag Coefficients of Spheres in Continuum and Rarefied Flows", AIAA Journal, Vol. 14, No. 6, pp. 707-708, (1976).

[17] Crowe, T. C., Babcock, R. W., Willoughby, G. P. and Carlson, L. R., "Measurement of Particle Drag Coefficients in Flow Regimes Encountered by Particles in a Rocket Nozzle", UTC 2296-FR, United Technology Center, (1968).

[18] Hermsen, R. W., "Review of Particle Drag Models", JANAF Performance Standardization Subcommittee 12th Meeting Minutes, CPIA, Vol. 113, (1979).